J. Fluid Mech. (2007), *vol.* 578, *pp.* 305–330.
doi:10.1017/S0022112007004867 Printed in the United Kingdom

Active control of high-speed and high-Reynolds-number jets using plasma actuators

M. SAMIMY, J.-H. KIM, J. KASTNER, I. ADAMOVICH AND Y. UTKIN

Department of Mechanical Engineering, GDTL/AARL; 2300 West Case Road, The Ohio State University, Columbus, Ohio 43235, USA

(Received 4 August 2006 and in revised form 8 November 2006)

Localized arc filament plasma actuators are used to control an axisymmetric Mach 1.3 ideally expanded jet of 2.54 cm exit diameter and a Reynolds number based on the nozzle exit diameter of about 1.1×10^6. Measurements of growth and decay of perturbations seeded in the flow by the actuators, laser-based planar flow visualizations, and particle imaging velocimetry measurements are used to evaluate the effects of control. Eight actuators distributed azimuthally inside the nozzle, approximately 1 mm upstream of the nozzle exit, are used to force various azimuthal modes over a large frequency range (St_{DF} of 0.13 to 1.3). The jet responded to the forcing over the entire range of frequencies, but the response was optimum (in terms of the development of large coherent structures and mixing enhancement) around the jet preferred Strouhal number of 0.33 ($f = 5$ kHz), in good agreement with the results in the literature for low-speed and low-Reynolds-number jets. The jet (with a thin boundary layer, $D/\theta \sim 250$) also responded to forcing with various azimuthal modes ($m = 0$ to 3 and $m = \pm 1, \pm 2, \pm 4$), again in agreement with instability analysis and experimental results in the literature for low-speed and low-Reynolds-number jets. Forcing the jet with the azimuthal mode $m = \pm 1$ at the jet preferred-mode frequency provided the maximum mixing enhancement, with a significant reduction in the jet potential core length and a significant increase in the jet centreline velocity decay rate beyond the end of the potential core.

1. Introduction

A planar free shear layer or mixing layer is a building block in many practical applications and thus has received much attention over the past several decades. Earlier studies of free shear flows had been stochastic in nature. The discovery of large-scale coherent structures in high-Reynolds-number free shear flows by Brown & Roshko (1974) and the subsequent realization that these structures play a major role in entrainment and bulk mixing changed the nature of the research and focused more attention on the dynamics and control of these structures. An excellent review article by Ho & Huerre (1984) details most of the early work on the physics of low-speed free shear flows as well as their control over about two decades. A further review article by Gutmark, Schadow & Yu (1995) details the work in high-speed free shear flows.

Planar free shear layers will be discussed briefly in the next section followed by a discussion of added complications associated with axisymmetric jets, which are the subject of this paper.

1.1. *Planar free shear layer*

It has been known for several decades that a free shear layer is unstable and acts like an amplifier of disturbances in the flow over a range of frequencies. The instability of free shear layers is referred to as Kelvin–Helmholtz instability. At sufficiently high Reynolds numbers, the effect of viscosity in the amplification of disturbances is relatively small, and thus the instability is also called inviscid instability. Detailed linear stability analyses (e.g. Michalke 1965, 1977) over the years have shown that the most amplified frequency scales with the momentum thickness of the boundary layer at the trailing edge of the splitter plate ($St_\theta = f_n\theta_0/U_\infty = 0.013$, where f_n is the most amplified frequency, θ_0 is the boundary layer momentum thickness, and U_∞ is the free-stream velocity). Subsequent experimental work not only confirmed the existence of such an instability mechanism and the scaling of f_n with θ_0, but also showed that the initial waves due to the Kelvin–Helmholtz instability mechanism roll up into large-scale structures (Brown & Roshko 1974). These structures entrain the fluid into the mixing layer from both sides and play a major role in the bulk mixing of the fluids. The structures then go through successive merging. Merging of a pair of structures results in further entrainment and mixing, production of Reynolds stresses, and doubling of the wavelength (e.g. Ho & Huerre 1984). In practice the size of the experimental facility will limit the number of sequential merging processes. Beyond sufficiently large Reynolds numbers, the state of the boundary layer on the splitter plate (i.e. laminar or turbulent) does not significantly alter the processes of vortex roll-up and subsequent merging. The processes taking place in the shear layer beyond the initial development of structures (i.e. roll-up and pairing) are nonlinear and beyond the reach of linear stability analysis.

In a mixing layer without any artificial excitation, natural disturbances are random in nature, and as a result there is jitter in the vortex roll-up and subsequent merging processes. Therefore, large-scale structures are not often spatially or temporally coherent and merging locations are not spatially fixed. By introduction of a low-amplitude forcing, the events could be manipulated and changed dramatically, and large-scale structures could be made much more organized (e.g. Winant & Browand 1974; Ho & Huang 1982). In a forced shear layer, the processes of vortex roll-up and subsequent merging will take place in an organized fashion. However, the merging could be delayed or promoted, depending upon the ratio of the forcing frequency to the most amplified frequency. If this ratio is quite small ($\sim 1/10$), simultaneous interaction of more than two structures could be promoted, in which case several structures are developed and initially displaced in the lateral direction and eventually merged together. Ho & Huang (1982) called this 'collective interaction'. The forcing level required for this process seems to be much higher than the level required for the promotion of just roll-up or pairing.

1.2. *Axisymmetric jets*

Owing to its wide engineering applications, in addition to scientific curiosity, numerous researchers have attempted to shed light on the physics of axisymmetric jets. Only a few of these works will be cited here. In an axisymmetric jet with a thin boundary layer leaving a nozzle, the effect of curvature is negligible and the initial shear layer

behaves similarly to the planar free shear layer. Further downstream, two additional complexities come into play. The first one arises from azimuthal modes in the shear layer, which compete with each other for energy and growth. The second one arises from the inward growth of the free shear layer towards the jet centreline and its eventual merging on the centreline, which ends the jet potential core.

The principal factor determining the growth rate and amplitude of azimuthal modes seems to be the ratio of the jet nozzle exit diameter to the boundary layer momentum thickness at the nozzle exit (D/θ_0). Linear stability analysis of Michalke (1977) and Plaschko (1979) and experimental work of Cohen & Wygnanski (1987), Corke, Shakib & Nagib (1991), and Corke & Kusek (1993) showed that for large D/θ_0 ($D/\theta_0 \gg 1$), both axisymmetric ($m = 0$) and the first spinning or helical modes ($m = +1$ or -1) are unstable in the initial jet shear layer. Linear stability analysis of Cohen & Wygnanski (1987) also showed that for a very thin boundary layer (or very large D/θ_0), many azimuthal modes are unstable in the initial shear layer region. Linear stability analysis of Michalke (1977) also showed that further downstream in the jet, where the velocity profile is bell-shaped, the jet can only support helical modes. It has also been reported that the growth region of helical modes move further upstream towards the nozzle as the jet velocity increases (Ho & Huerre 1984).

As was mentioned earlier, the sequential merging processes in planar shear layers could last as long as the experimental geometry permits. The interaction between two large-scale structures, resulting in pairing, takes place as the downstream structure slows down and the upstream structure speeds up (e.g. Ho & Huerre 1984). However, in an axisymmetric jet, the inward growth of the jet shear layer and its merging on the jet axis ends the typical growth and interaction and starts an additional interaction, known as azimuthal interaction. The average location at which the jet centreline velocity begins decaying is called the end of jet potential core. This interaction, which is dynamic and nonlinear, adds great complexity to the problem. Linear stability analysis, which has been fundamental in the understanding of free shear layers is applicable only in the early development of the shear layer up to roll-up.

Many researchers have shown experimentally that the passage frequency of large-scale structures at the end of the potential core, called the preferred mode or jet column mode frequency, is scaled with the nozzle exit diameter ($St_D = f_p D/U_j \sim$ constant, where f_p is the jet column frequency and U_J is the jet exit velocity) (e.g. Crow & Champagne 1971; Zaman & Hussain 1980; Reynolds & Bouchard 1981; Hussain & Zaman 1981). St_D seems to vary over a large range (from about 0.2 to 0.6), but mostly remains around 0.3 (Ho & Huerre 1984). The variations have two main sources (Gutmark & Ho 1983). The first one is non-physical and related to where in the jet and how the frequency is measured. The second one is physical and related to the dominant disturbances in a given facility. The pseudo-non-linear stability analysis of Crighton & Gaster (1976) puts this mode around $St_D = 0.4$.

From what has been discussed so far, it is clear that the jet preferred mode, f_p, must be related to the most amplified shear layer mode, f_n, by $f_n/f_p = 2^n$, where n, typically 3, is the number of pairings taking place before the end of the potential core. This proportionality seems to hold in low-speed flows with large boundary layer momentum thickness as demonstrated by Kibens (1980) in an acoustically forced jet, but locks onto a fixed frequency at higher velocities (Ho & Huerre 1984). The reason for this locking is not clear. Hussain & Zaman (1981) reported that in jets forced at the preferred mode frequency, the structures have locked onto this frequency by 2 to 3 nozzle diameters downstream, and there is no tendency for pairing or sub-harmonic growth. They also reported that the characteristics of large-scale structures

at the preferred mode are independent of the state of the boundary layer exiting the nozzle (i.e. laminar or turbulent). But, as the Reynolds number is increased, the structures become more round (shorter in x and wider in y), which means more lateral momentum transport.

It is not clear from the literature how to get from the most amplified mode (or structure) to the preferred mode (structure) in axisymmetric jets. There are three potential routes. The first one is the typical growth and roll-up of the most amplified mode and then sequential pairing, as they occur in planar shear layers. The second potential route is a bypass-type process, in which a wave at the preferred frequency grows and rolls up. A similar type of process is known to take place in a boundary layer transition to turbulence (e.g. Reshotko 1994). The third potential process could involve the 'collective interaction' seen in planar shear layers (Winant & Browand 1974 and Ho & Huang 1982), in which more than one pair of vortices interact and merge. It is known that forcing the preferred mode of a jet requires higher forcing amplitude, which is also true in the collective interaction case. It is also known that higher-amplitude disturbances in the boundary layer lead to bypass transition. Therefore, either one of the last two routes seems quite plausible.

Various methods to control axisymmetric jets will first be discussed in the next section. The focus will then be on the use of plasma actuators for jet control.

1.3. *Control of axisymmetric jets*

Flow control in general is divided into two categories: passive and active. In the former, the control is accomplished by geometrical modifications to the nozzle. In the latter, some energy (in the form of heat, mass and/or momentum) is added to the flow. Active control is further divided into open-loop and closed-loop control. In open-loop control, actuation takes place based on the operator's command or a predetermined and tabulated input. In closed-loop control, information from a sensor or sensors in the flow along with a flow model guides the actuation process. Only passive control and active open-loop control will briefly be discussed below.

There has been a surge in interest in the passive control of jets in recent years, primarily motivated by noise mitigation. Passive control of jets and mixing layers is accomplished via geometrical modifications of the nozzle/splitter-plate trailing edge using tabs, chevrons, and lobbed nozzles (e.g. Samimy, Zaman & Reeder 1993; Zaman, Reeder & Samimy 1994; Zaman 1999; Mengle 2000; Saiyed, Mikkelsen & Bridges 2003; Callender, Gutmark & Martens 2005). The main mechanism in controlling the jet using these passive techniques is streamwise vorticity generated by the geometrical modifications (Zaman *et al.* 1994).

Open-loop active control can be divided into two categories. The first category involves steady or low-frequency (frequency much lower than any instability frequency in the flow) energy addition to the flow. A few examples include steady fluidic injection through micro-jets (Arakeri *et al.* 2003 and Krothapali *et al.* 2003), fluidic chevrons (Henderson *et al.* 2005), and some recent unpublished work on active chevrons using shape memory alloy. The second category involves using actuators with frequency capabilities in the range of the flow instability frequencies. This is the subject of the current work and will be further discussed next.

As was discussed earlier, the initial motivations for exciting instabilities of mixing layers and jets with low-amplitude forcing were to regularize roll-up and subsequent pairing to aid flow diagnostics for physical understanding of these processes. The goal was changed in later years to controlling these flows with a specific goal of mixing enhancement and/or noise mitigation. Numerous researchers have worked in this area,

but only a few will be mentioned here. Most of these investigations have been carried out in relatively low-speed and low-Reynolds-number jets (e.g. Crow & Champagne 1971; Kibens 1980; Hussain & Zaman 1980; Zaman & Hussain 1981; Ho & Huerre 1984; Cohen & Wygnanski 1987). A few investigations have also been carried out in high-speed but still low-Reynolds-number jets by performing the experiments in a low-pressure chamber (e.g. Morrison & McLaughlin 1979; Stromberg, McLaughlin & Troutt 1980). Some researchers have also used more than one mode to enhance control effects (e.g. Cohen & Wygnanski 1987; Corke & Kusek 1993; Paschereit, Wygnanski & Fiedler 1995; Parekh *et al.* 1996; Reynolds *et al.* 2003).

Many researchers over several decades have contributed to the control of low-speed and low-Reynolds-number jets and to the understanding of the physics and mechanisms of jet response to such control. The upper limit of the Reynolds number based on jet diameter seems to be around 50 000 for the majority of these works. As the speed and the Reynolds number of the jet increase, so do the background noise, the instability frequencies, and the flow momentum. Therefore, actuators must provide excitation signals of much higher amplitude and frequencies-two opposing requirements. As a result, there is practically no work in the active control of high-speed and high-Reynolds-number jets, with only a few exceptions. For example, Kibens, Dorris III & Smith (1999) used high-amplitude pulsed injection to excite the exhaust from a full-scale jet engine at a flapping mode. They used two actuators, operating 180° out of phase and each covering a 1/4 of the jet perimeter. This resulted in significantly increased mixing and far-field noise radiation. Obviously, the increased scale and thus the reduced frequency (∼135 Hz) was a key factor in the implementation of actuation in this work. Also, Moore (1977), Jubelin (1980), Ahuja, Lepicovsky & Burrin (1982), Lu (1983), and Lepicovsky & Brown (1989) used acoustic forcing (either channelling the acoustic signal to multiple locations at the proximity of the exit of the jet or using it in the jet settling chamber) to force a high subsonic jet around its preferred mode, with some success.

We have recently developed a class of plasma actuators, called localized arc filament plasma actuators (LAFPA) that can provide excitation signals of high amplitude and high bandwidth for high-speed and high-Reynolds-number flow control (Samimy *et al.* 2004; Utkin *et al.* 2007). The actuator frequency, phase, and duty cycle can be controlled independently. Therefore, several of these actuators can be used to excite jet column modes, shear layer instability modes, and their various azimuthal modes. In the following sections, we will first provide a brief background on plasma-based actuators in general, then on LAFPA in particular.

1.4. *Plasma-based actuators for flow control*

In recent years, there has been considerable interest in the use of electric discharge plasmas for flow control. Over the last decade, the work in this field has covered a wide range of specific experimental approaches and engineering applications. In particular, various types of surface and volume-filling plasmas, including DC, AC, RF, microwave, arc, corona, and spark electric discharges, as well as laser-induced breakdown, have been used to modify flows. Applications of the plasma-assisted flow control mainly focus on viscous drag reduction and boundary layer separation control in low-speed flows, shock wave modification and wave drag reduction in supersonic flows, and supersonic boundary layer transition control. The primary mechanisms of plasma flow control include electrohydrodynamic (EHD) and magnetohydrodynamic (MHD) interactions, and thermal (Joule) heating. EHD and MHD interactions

involve flow entrainment by collisional momentum transfer from charged species accelerated by Coulomb and Lorentz forces.

The main limitation on the use of EHD flow control is generating significant ion densities in the cathode sheath (space charge region) of the discharge. Simple estimates (Macheret, Shneider & Miles 2004) show that a significant EHD effect on the boundary layer flow can be achieved at flow velocities of up to $U_\infty \sim 30$–$100\,\mathrm{m\,s^{-1}}$. This is consistent with experimental results on EHD airfoil flow separation control, demonstrated at $U_\infty \sim 1$–$10\,\mathrm{m\,s^{-1}}$ (Roth, Sherman & Wilkinson 2000; Corke & Matlis 2000; Artana *et al.* 2002), $U_\infty \sim 10$–$30\,\mathrm{m\,s^{-1}}$ (Post & Corke 2004), and $U_\infty \sim 20$–$75\,\mathrm{m\,s^{-1}}$ (Zavialov *et al.* 2005). As a result, the use of EHD for high-speed flow control (with flow velocities of a few hundred $\mathrm{m\,s^{-1}}$ or higher) appears to be impractical. For MHD flow control, the main limitation is sustaining significant flow conductivity. At $U_\infty \sim 1000\,\mathrm{m\,s^{-1}}$ and conductivity of $\sigma \sim 0.1\,\mathrm{mho\,m^{-1}}$, currently achieved in low-temperature unseeded air flows (Nishihara *et al.* 2005), the MHD effect in the free stream is significant only at low pressures, $P \sim 0.001$ atm (P ~ 0.04 atm in the boundary layer flow). These estimates are consistent with attempts to control low-speed salt-water flows ($\sigma \sim 1.0\,\mathrm{mho\,m^{-1}}$, $U_\infty \sim 1\,\mathrm{m\,sec}$, $\rho = 1\,\mathrm{kg\,cm^{-3}}$) (Henoch & Stace 1995) and Mach 3 air flows ($\sigma \sim 0.1\,\mathrm{mho\,m^{-1}}$, $U_\infty \sim 500\,\mathrm{m\,s^{-1}}$, $P \sim 0.01$ atm) (Nishihara *et al.* 2005). Sustaining higher conductivities using non-equilibrium plasmas requires prohibitively high-plasma power and is also limited by ionization instabilities. Thus, the use of MHD for high-speed flow control at near-atmospheric pressures also appears impractical, except perhaps for extremely high-temperature flows (Bobashev *et al.* 2003).

Thermal bulk heating plasma flow control attempts have used diffuse non-equilibrium plasmas (Mishin, Serov & Yavor 1991) or localized plasma torches or pulsed lasers ('airspike') (Minucci *et al.* 2005) to modify shock waves in front of a supersonic vehicle to reduce wave drag. Bulk heating of the high-speed flow by the plasma requires very high power (comparable to the flow enthalpy) and is also limited to low pressures (0.001–0.04 atm) due to plasma instabilities. Recent work by Leonov *et al.* (2002, 2003, 2004) suggests that significant high-speed flow control could be realized using the thermal effects of near-surface high-current high-temperature arc discharges. Intense, localized, rapid heating produced by plasmas in high-current pulsed electric discharges (similar to pulsed optical discharges, Adelgren *et al.* 2005*a*, *b*) produces shock waves, which have the control ability needed to modify the supersonic flow over blunt bodies. In this approach, rapid near-adiabatic heating in the current filament results in a pressure jump, which we have demonstrated capable of forcing instabilities in high-Reynolds-number jets.

Unlike other approaches, the method used in the present work does not require the use of high-power lasers, microwave beams, or electrodes protruding into the flow. The proximity of the arc plasma to the wall improves its stability and prevents plasma blow-off by the high-speed flow. The high-current, high-temperature, localized arc discharge is completely different from low-temperature, low-current, diffuse glow discharges used in previous low-speed flow control work (Roth *et al.*; Wilkinson 2000; Post & Corke 2004). In our approach, the flow is affected by localized perturbations produced by arc-generated pressure/temperature spikes (a purely thermal effect). The present approach is not limited to low-speed flows (unlike EHD control) or low-pressure flows (unlike MHD control), and at the same time it requires low enough energy to be integrated on aircraft. In fact, the present approach remains the only energy-efficient, high-speed, standard (∼sea level) static pressure flow control method that has been demonstrated in experiments.

2. Experimental facility and techniques

The experimental facility and techniques utilized in the current research will now be described. The presentation will include flow facility, flow diagnostic techniques, and the plasma actuators, including their power supply and control system.

2.1. *Flow facility*

All the experiments were conducted in the Gas Dynamics and Turbulence Laboratory at The Ohio State University. The ambient air is compressed, dried, and stored in two cylindrical tanks at a pressure of up to 16 MPa with a capacity of 36 m^3. The compressed air is supplied to the stagnation chamber and conditioned before entering a Mach number 1.3 axisymmetric converging–diverging nozzle, which is designed using the Method of Characteristics for uniform flow at the nozzle exit. The air is discharged horizontally through the nozzle into an anechoic chamber. The nozzle has an exit diameter of 2.54 cm (1.0 in). For the Mach 1.3 jet, the jet preferred mode frequency should be around 5 kHz, assuming $f_p D/U_\infty = 0.3$, which agrees quite well with the experimental results that will be presented in § 3. An extension, made of boron nitride, was attached to the exit of the nozzle to house the plasma actuators.

The Mach number of the jet at the nozzle exit was measured to be 1.3 and the Reynolds number based on the jet diameter was about 1.1×10^6. The jet was operated as close to the pressure-matched ideally expanded condition as possible. However, because of the nozzle extension to accommodate plasma actuators, which generates a very thick nozzle lip, we observed variation in the centreline Mach number within the jet core region, indicating a weak shock/expansion train. The boundary layer thickness at the exit of the nozzle is very thin, making it impossible to obtain a boundary layer profile to estimate its momentum thickness and its state. Kastner, Hileman & Samimy (2004) attached a converging nozzle of similar length to this facility and measured a few points within the boundary layer of a Mach 0.9 jet with a Reynolds number about 0.76×10^6. They estimated the boundary layer to be turbulent with a thickness of about 1 mm and a momentum thickness of about 0.1 mm. The characteristics of the boundary layer in the current experiments are expected to be quite similar. Assuming an initial momentum thickness of 0.1 mm for the Mach 1.3 jet and $St_\theta = f_n\theta_0/U_\infty = 0.013$, the initial shear layer most-amplified frequency is around 50 kHz. It would be around 40 kHz if three successive pairings of large-scale structures had taken place to decrease the passage frequency to the preferred mode frequency of about 5 kHz by the end of the jet potential core.

2.2. *Flow diagnostic techniques*

The growth and decay of perturbations imparted to the flow by the plasma actuators were measured by a Kulite pressure transducer probe. The probe was a small round cylinder with the Kulite transducer mounted at the tip and axis normal to the jet axis so that the instantaneous static pressure – rather than total pressure – was measured. The probe tip was located at the lip-line of the nozzle radially, at the centre of actuator 7 (figure 1) azimuthally, and traversed in the streamwise direction manually from $x/D = 0.5$ to 10.5. The signal from the probe was amplified, low-pass filtered, and stored on a PC. An average spectrum was obtained from one hundred short-time spectra for each case and the perturbation level at the forcing frequency was calculated from the average spectrum. For the baseline case, the level was obtained at a frequency matching the forcing frequency. The perturbation level was normalized by 2×10^{-5} Pa in all cases.

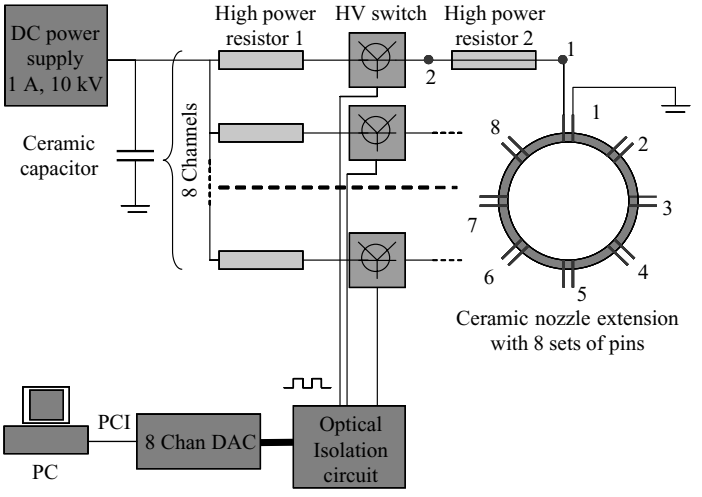

FIGURE 1. Schematic of the in-house fabricated plasma generator.

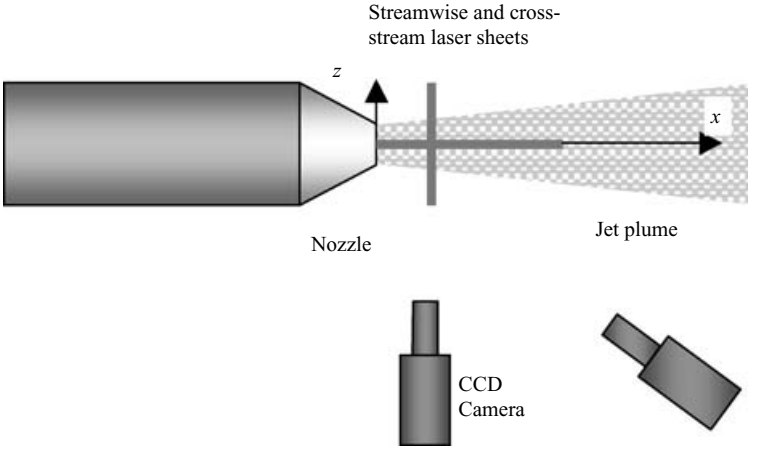

FIGURE 2. Schematic of the baseline jet and the PIV and planar flow visualization set-up. Y-direction is normal to the page.

The flow was visualized using scattering of light from a laser sheet passing through the centreline of the jet (streamwise sheet) or normal to the jet axis (cross-stream sheet) (figure 2). The light-scattering particles were formed in the mixing layer of the jet when the moist and warm ambient air was entrained into the jet and mixed with the cold but dry jet air. Either a Spectra Physics Quanta-Ray Pro or PIV-400 Nd:YAG laser was used as a light source. The scattered laser light was captured by a Princeton Instrument Pixis CCD camera, located normal to the laser sheet for streamwise images and with an angle of about 30° to the laser sheet for cross-stream images (figure 2). Instantaneous planar images of the jet with 9 ns exposure time (the laser pulse duration) were acquired. In this visualization technique, a major portion of the mixing layer is visualized since no condensation occurs in the jet core or the ambient air.

The images of the jet were taken either randomly or phase-locked to the input signal to the transistor switch of an actuator. A 10 Hz TTL signal generated by a

pulse counter, phase-locked to the input signal, was directed to the laser lamp-trigger input and the laser lamp-sync output was used to trigger the camera. A custom-built circuit was used to isolate laser and imaging systems from the TTL signal to the transistor switches.

Particle imaging velocimetry (PIV) was used to measure the x and y components of velocity on the illuminated (x, y)-plane (figure 2). Images were acquired and processed using a LaVision PIV system with a 2000 by 2000 pixels Redlake CCD camera employing a 75–300 mm Vivitar zoom lens with a 532 nm narrow band optical filter. Other essential hardware and software are housed in a dedicated computer with dual Intel Xeon processors. The system triggers a dual-head Spectra Physics PIV-400 Nd:YAG laser operating at the second harmonic (532 nm). Each laser head was operated at approximately 350 mJ per pulse for PIV applications. Image pairs were acquired at a sampling rate of approximately 5 Hz.

The jet flow was seeded with di-ethyl-hexyl-sebacat (DEHS) fluid introduced upstream of the stagnation chamber by a four-jet atomizer. This location was chosen to provide a homogenous dispersion of the particle seed throughout the jet. A free jet entrains a significant amount of ambient air. The ambient air was seeded by injecting fog from a fog generator into a 15 in. diameter cylinder located symmetrically around the jet and a small amount of air was introduced to generate a very low-speed co-flow. The camera views the streamwise laser sheet orthogonally over about 9 jet diameters as in the flow visualization case. The time separation between laser pulses was 2.0 ms for images divided into 32 by 32 pixel interrogation windows. Sub-regions for each image pair were cross-correlated using multi-pass processing with a 50 % overlap in order to improve spatial resolution and to prevent the appearance of spurious vectors by adaptively improving the window size. Initial passes used 64 by 64 pixel interrogation windows, which were then used as a reference for the 32 by 32 pixel windows in the final pass. This experimental set-up produced a velocity vector grid of 115 by 65 over the measurement domain. With this arrangement, two adjacent velocity vectors are separated by approximately 2 mm.

2.3. *Plasma actuators and plasma generator system*

Each actuator consists of a pair of pin electrodes. The electrodes are distributed around the nozzle perimeter (figure 1), approximately 1 mm upstream of the nozzle exit plane. A ring groove 0.5 mm deep and 1 mm wide was used to house the electrodes and to shield and stabilize the plasma. Without such a groove the plasma was swept downstream by the flow. For the work presented here, the nozzle extension was made of boron nitride and steel or tungsten wires of 1 mm diameter were used for electrodes. Tungsten wires have proven to be more resistant to the erosion caused by the arc discharge. The spacing between a pair of electrodes for each actuator, measured centre-to-centre, is 3 mm.

Figure 1 shows a schematic of the multi-channel high-voltage plasma generator, designed and built in-house at The Ohio State University. The plasma generator enables simultaneous powering of up to eight localized arc filament plasma actuators distributed around the perimeter of the ceramic nozzle extension, with independent frequency, duty cycle, and phase control of individual actuators. Each actuator is connected in series with a fast-response, high-repetition-rate, high-voltage switch, two approximately 15 kΩ high power solid-body ceramic ballast resistors, and a high-voltage, high-current (10 kV, 1 A) DC power supply. Two of these power supplies are used to energize the eight actuators. If all eight actuators are powered at the same time, the single actuator current is limited to 0.25 A. The switches are controlled

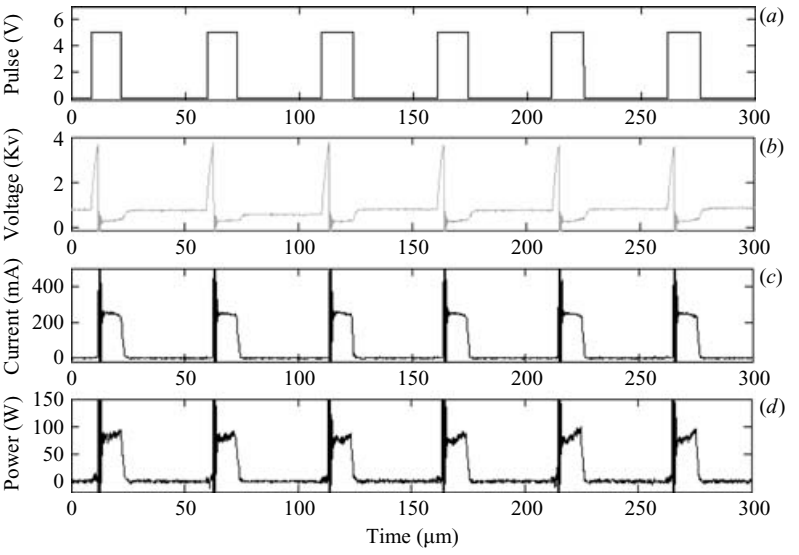

FIGURE 3. Input rectangular pulse to a plasma actuator and time-dependent voltage, current, and power of the actuator operated at 20 kHz frequency and 20% duty cycle (only one actuator was operated).

by using an 8-channel digital-to-analog output PCI card and the LabView software, which allows independent frequency, duty cycle, and phase control. The switches are capable of producing high-voltage pulses (up to 10 kV) at repetition rates from a few Hz to 200 kHz, with a very short pulse rise/fall time ($\sim 0.1\,\mu s^{-1}$) and a variable duty cycle (from 0 to 100 %). With eight actuators uniformly distributed around the perimeter of the nozzle, azimuthal modes (m) 0, 1, 2, 3, ± 1, ± 2, ± 4 can be forced.

By turning the electronic switch on and off, positive high-voltage pulses can be applied to the corresponding actuator. The high initial voltage is needed to produce breakdown in the approximately atmospheric pressure air in the gap between the two electrodes of an actuator, which are 3 mm apart in the present work. After the breakdown, the arc is generated and the voltage across the gap rapidly falls to a few hundred volts. Every switch is liquid cooled to allow continuous operation at high frequency, voltage and current. The plasma generator is compact, robust, and simple to operate. In the present work, continuous operation of all eight actuators in a Mach 1.3 flow (up to several minutes) has been achieved. To reduce the EMI interference with the computer and data acquisition board an in-house-built optical isolation circuit was implemented on the low-voltage side.

3. Experimental results and discussion

Experimental results are presented in this section, and discussed in the following order: characterization of plasma actuators, development of actuation perturbation and instability wave/large-scale structure growth, flow visualization images, and PIV results.

3.1. *Plasma actuator characterization*

Figure 3 shows the input rectangular wave to a plasma actuator, time-dependent voltage, current, and power in the arc discharge between two steel wire electrodes of the actuator. During these measurements, eight actuators were operated in the first

helical mode at 20 kHz frequency and a 20 % duty cycle in the ideally expanded Mach 1.3 jet. The static pressure at the actuator location (1 mm before the nozzle extension exit) was approximately 1 atm. Figure 3(*b*) shows the time-dependent voltage between the actuator electrodes, measured at the HV pin electrode (see figure 1) by an Agilent high-voltage probe N2771A. A very large voltage overshoot (about 4 kV) at the onset of the cycle ($t \approx 10\,\mu s^{-1}$ on the graph) corresponds to electrical breakdown in the air between the electrodes, followed by a sharp voltage drop to about 500 V, as a stationary arc discharge is formed. After the discharge current is interrupted by rapidly closing the switch ($10\,\mu s^{-1}$ later), the plasma is quickly blown off by the flow. Because of this, the high-voltage electrode (anode) becomes floating and the voltage remains essentially unchanged (at about 500 V) until the moment the switch is opened again $40\,\mu s^{-1}$ later.

The actuator current was measured simultaneously with the voltage using a LeCroy CP031 current probe and shown in figure 3(*c*). The current trace is nearly a step function, with the steady-state current of about 0.25 A when the switch is open and no current when it is closed. The time-dependent arc discharge power can be obtained by multiplication of the current and the voltage traces. The result is shown in figure 3(*d*). The power during the current pulse reaches approximately 100 W, which corresponds to a time-averaged actuator power of only 20 W (i.e. 160 W net power for all eight actuators in operation). For comparison, the flow power (the total enthalpy flux) at these conditions is about 28 kW – a ratio of the average actuator to the flow power of 0.57 %. These results demonstrate that high-speed flow control by localized arc plasma actuators can be highly energy efficient. Note that the power generated by the DC power supply used to run the plasma actuators in the present work is significantly higher, approximately 400 W time-averaged power per actuator at the conditions of figure 3, with more than 90 % of the power dissipating on the ballast resistors. However, the use of a more efficient plasma generator producing a periodic, low-voltage, rectangular waveform, with short high-voltage pulses to achieve breakdown at the beginning of each period would greatly reduce the power budget of the entire flow control system.

The measurements showed that the voltage, current, and power traces for all eight actuators are essentially the same except for a phase shift. Depending on the frequency, mode, and duty cycle, the arc discharges produced by different actuators may overlap in time. It can be seen in figure 3 that the actual duty cycle was somewhat smaller than 20 % due to a delay between the square-wave input signal (figure 3*a*) and the resultant high-voltage output. The delay is caused by the combined capacitance of the switch, resistors, high-voltage cables, and electrodes.

The actuators can operate over a wide range of frequencies (a few Hz to 200 kHz), far beyond the jet column instability (~5 kHz) and the initial shear layer instability (~50 kHz). Using eight plasma actuators, as shown in figure 1, one can force azimuthal modes (m) 0, 1, 2, 3, ±1, ±2 and ±4. Traditionally, when distributed acoustic drivers were used for excitation, the input amplitude, A_a, for a given azimuthal mode was given by

$$A_a = A_o \sin(2\pi f_F t - m\phi_a) \tag{3.1}$$

where f_F is the forcing frequency, t is time, m is the azimuthal mode, and ϕ_a is the azimuthal location of the actuator. The subscript a represents the actuator number (1 to 8), for example in figure 1, $\phi_1 = 0$, $\phi_2 = \pi/4$, etc.

The input for the LAFPA is different to that for an acoustic driver because a rectangular pulse sequence is used instead of a sine wave. The pulse train has a frequency

and a phase, as in a sine wave, but it also has a duty cycle. The input to a plasma actuator for a given azimuthal mode is given by

$$A_a = A_o g(2\pi f_F t - m\phi_a) \text{ with } g(2\pi f_F t - m\phi_a) = \begin{cases} 1 & \text{if } 0 < 2\pi f_F t - m\phi_a < 2\pi\delta \\ 0 & \text{if } 2\pi\delta < 2\pi f_F t - m\phi_a < 2\pi. \end{cases} \tag{3.2}$$

The step function, $g(t)$, is either 0 or 1 based on the duty cycle, δ, the actuator location, ϕ_a, and the forcing frequency, f_F. The step function can also be written in the time domain:

$$g(t) = \begin{cases} 0 & \text{if } 0 < t < m\phi_a/2\pi f_F \\ 1 & \text{if } m\phi_a/2\pi f_F < t < \delta/f_F + m\phi_a/2\pi f_F \\ 0 & \text{if } \delta/f_F + m\phi_a/2\pi f_F < t < 1/f_F. \end{cases} \tag{3.3}$$

A detailed investigation into the active control of an Mach 1.3 ideally expanded axisymmetric jet using eight actuators at a prescribed frequency and azimuthal mode has been carried out. The results are presented and discussed in the following sections.

3.2. *Development of actuation perturbations and the instability waves/large-scale structures*

A dynamic Kulite pressure transducer was used to measure time-resolved pressure in the ideally expanded Mach 1.3 jet to explore the development of the perturbations seeded in the flow by plasma actuators and the instability waves/large-scale structures. The cylindrical probe with the transducer on the tip of it, located at the same azimuthal location as actuator number 7 in figure 1, normal to the jet centreline, was traversed in the streamwise direction from $x/D = 0.5$ to 10.5. The tip of the probe grazes the shear layer at the first measurement location ($x/D = 0.5$), but is well into the shear layer farther downstream, as the shear layer is growing. The amplitude of the local dynamic pressure at the forcing frequency was obtained using the power spectrum of the time-resolved Kulite pressure signal.

Since eight actuators were distributed around the nozzle exit, we could force azimuthal modes from $m = 0$ (axisymmetric mode) to $m = \pm 3$ (third helical or spinning) mode, in addition to $m = \pm 1$, ± 2, or ± 4 modes. The jet was forced over a frequency range of 2 kHz to 20 kHz (St_{DF} from 0.13 to 1.31). The excitation frequency effect is shown in figure 4, which depicts the spatial development in the streamwise direction of the seeded perturbations at several Strouhal numbers when the jet is forced at three azimuthal modes of $m = 0$, 1, and ± 1. For the last case, the measurement is on the excitation or flapping plane of the jet. As the forcing Strouhal number increases from 0.13 toward 1.31, several trends are observed: (i) the perturbation amplitude at the first measurement point ($x/D = 0.5$) keeps increasing (ii) the maximum amplitude achieved for each perturbation follows a similar trend; (iii) the location of the onset of the perturbation decay moves upstream; and (iv) the trends for all three azimuthal mode excitation cases are similar. For example, for the axisymmetric excitation, the perturbation amplitude at the first measurement location, the maximum achieved amplitude, and the location for the onset of decay after the peak saturation for forcing at St_{DF} ($= f_F D/U_J$, where f_F is the forcing frequency) of 0.13 are 132 dB, 150 dB, and $x/D \sim 4$, respectively; and at St_{DF} of 1.13 they are 172 dB, 172 dB (or higher), and $x/D = 0.5$ (or upstream). This is related to matching of the excitation wavelength to the local instability wavelength. We will further discuss this issue later when we present flow visualization results. Moore (1977) performed similar

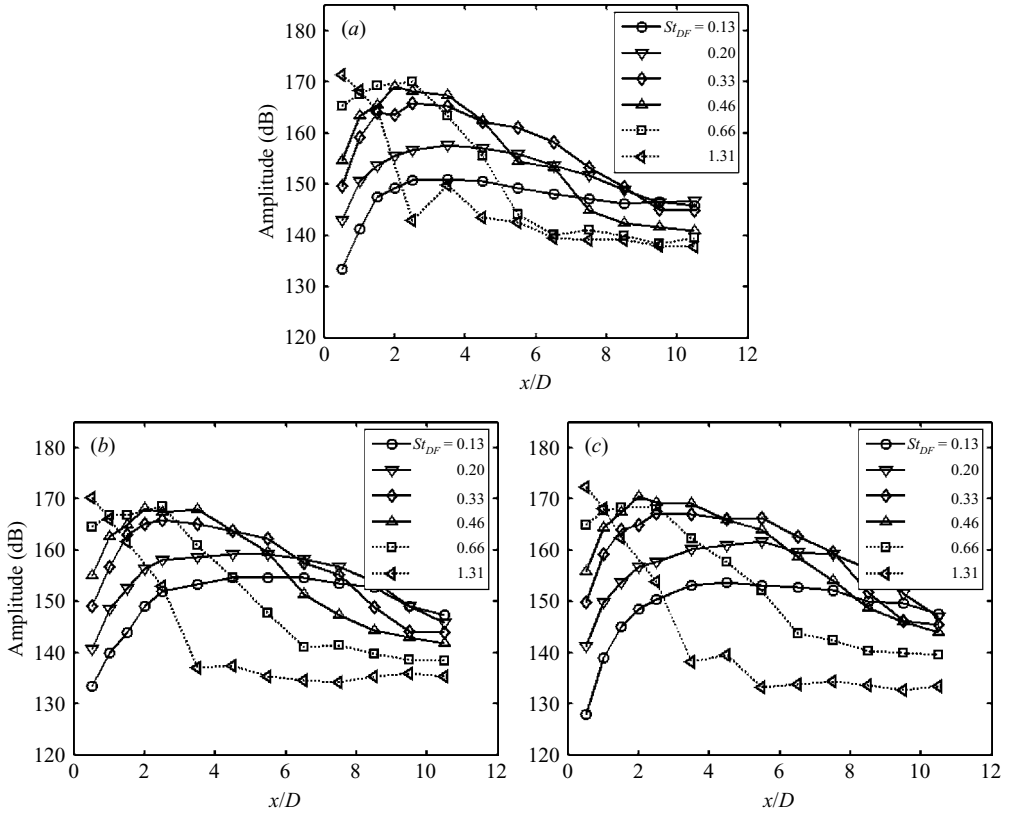

FIGURE 4. Effects of excitation Strouhal number on the spatial development of a seeded perturbation for azimuthal mode. (*a*) $m = 0$, (*b*) 1, and (*c*) ± 1 (on the excitation plane). The perturbation was normalized by 2×10^{-5} Pa.

experiments using an acoustic driver to excite the jet preferred frequency in a low-Mach-number jet. The maximum perturbation amplitude occurred between $x = 2D$ and $4D$ with amplitudes around 160 dB, which is very similar to the present results.

Figure 5 shows the spatial development of the seeded perturbations and the instability waves/large-scale structures at three different Strouhal numbers ($St_{DF} = 0.13,\ 0.33,\ 0.66$) when the jet is forced at various azimuthal modes ($m = 0, 1, 2, 3, \pm 1$). For comparison, the results for the baseline case (unforced case) and also a case in which only a single actuator (actuator 7 in figure 1) operaties are shown. Note that there is no external perturbation in the baseline case, but there are always natural and random disturbances in the flow. The trend, as expected, is gradual growth and saturation at lower frequencies and rapid growth and saturation at higher frequencies. For the various azimuthal forcing cases, some interesting observations can be made. For example, (i) regardless of the forcing frequency, higher azimuthal modes saturate earlier and decay faster; (ii) all perturbations approach the baseline farther downstream; (ii) there is a strong competition between the axisymmetric and first helical modes – the latter seem to be winning in the lower frequencies and the former in the higher frequencies; and (iv) the growth and decay of the seeded perturbation levels are less dependent on the azimuthal modes at a higher frequency of 20 kHz, which is not shown here. For the thin boundary layer ($D/\theta_0 \gg 1$) exiting the nozzle in the present work, these results are consistent with the linear stability

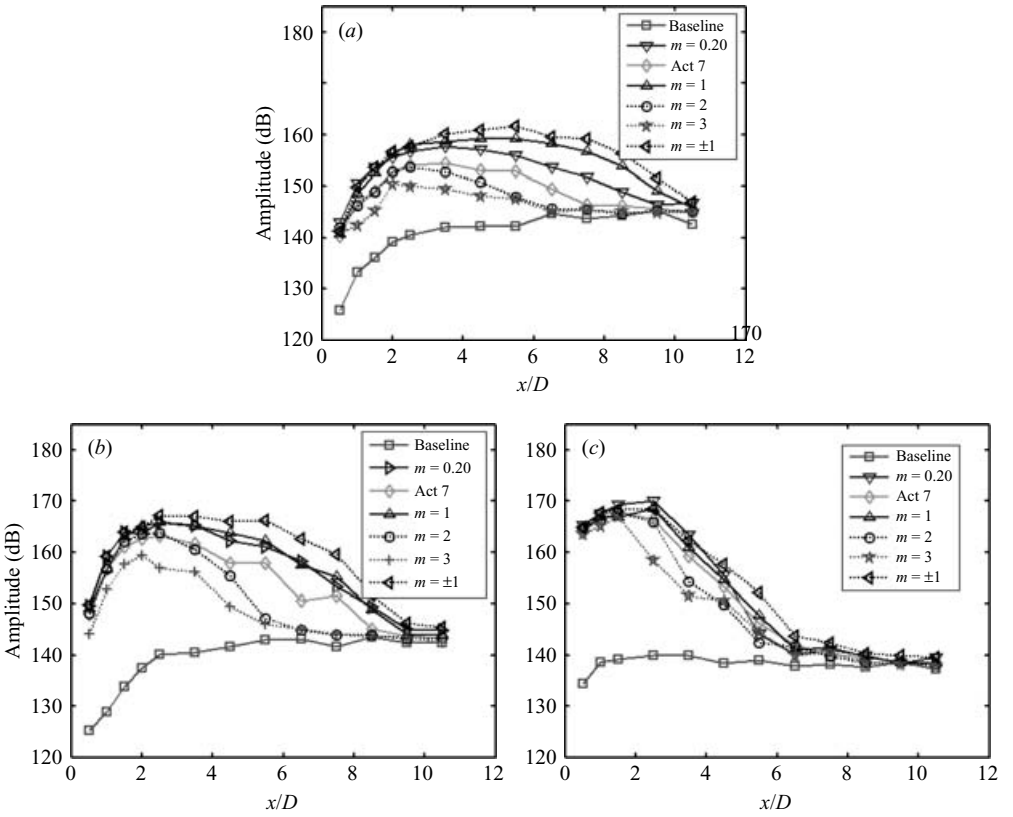

FIGURE 5. Effects of excitation modes on the spatial development of a seeded perturbation for (*a*) $St_{DF} = 0.13$, (*b*) 0.33, and (*c*) 0.66 (on the excitation plane). The perturbation was normalized by 2×10^{-5} Pa.

analysis of Michalke (1977), Plaschko (1979) and Cohen & Wygnanski (1987) and experimental work of Cohen & Wygnanski (1987), Corke *et al.* (1991), and Corke & Kusek (1993). The energy exchange between various azimuthal modes and the mean flow seems to be similar in the instability wave/perturbation growth phase, but significantly different in the decay phase – the higher azimuthal modes decay much faster, especially for lower Strouhal number forcing. We were limited to $m = 3$ with the current eight actuators arrangement. We will use more actuators, enabling us to excite higher azimuthal modes, in the near future.

3.3. *Flow visualization results*

Figure 6 shows a typical instantaneous image with 9 ns exposure time and an ensemble-averaged image of the baseline Mach 1.3 jet. Thirty instantaneous images were used to obtain the ensemble-averaged image. The distance between two adjacent tick marks in the images is one nozzle exit diameter and the first tick mark is at $1D$ from the nozzle exit. Only the mixing layer of the jet is visualized. Mixing between the cold and dry jet air with the entrained warmer and humid ambient air generates particles of order 50 nm in diameter for laser light scattering. The instantaneous image shows large-scale structures in the mixing layer, which are not spatially or temporally coherent, typical of those in high-Reynolds-number and high-speed jets and mixing layers. The ensemble-averaged image is of course featureless and shows the growth

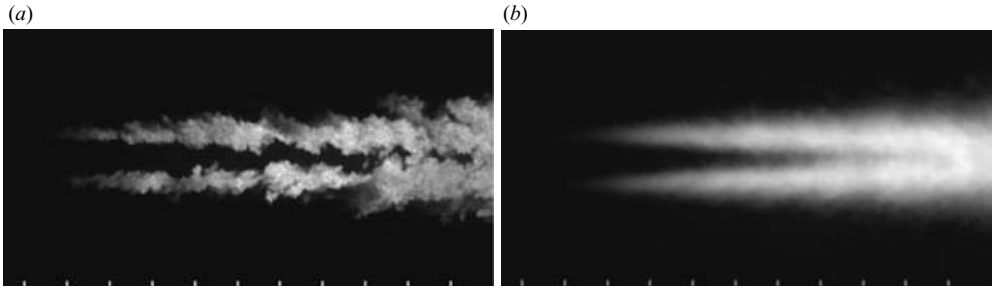

FIGURE 6. Instantaneous (*a*) and (*b*) ensemble-averaged streamwise images for the baseline jet. The tick mark spacing is one diameter and the first tick mark indicate is at $x/D = 1$.

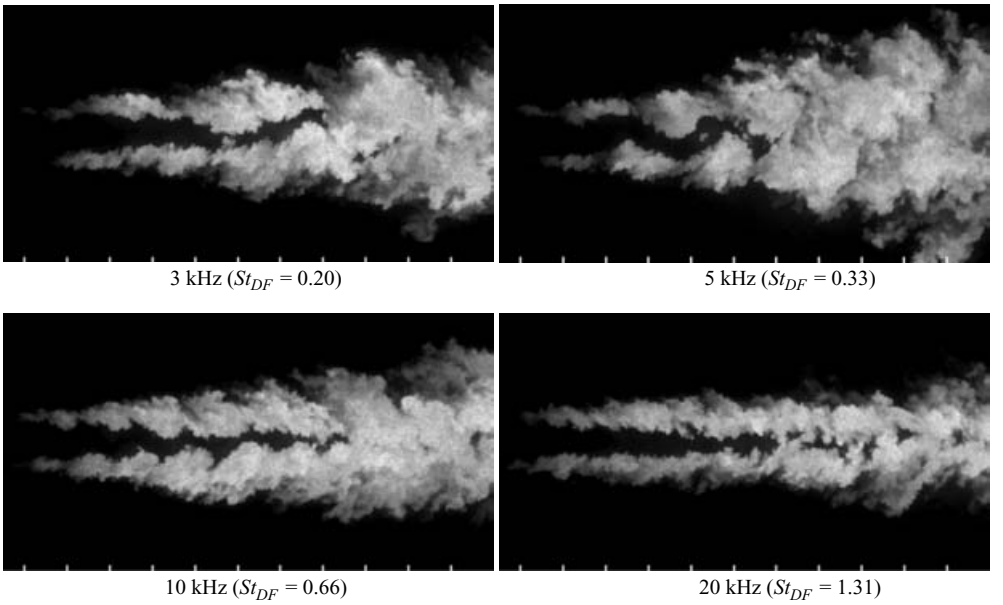

FIGURE 7. Effects of the forcing frequency with the flapping mode ($m = \pm 1$).

of the mixing layer, both inward and outward, in the downstream direction from the nozzle exit. The ensemble-averaged image shows the end of the *visual* potential core around at $7D$ from the nozzle exit, which would change to some degree depending on the ambient air moisture level. Earlier Pitot probe measurements (Hileman *et al.* 2005) and the PIV measurements to be presented the later in the paper showed the end of potential core for the baseline jet to be located around $6D$.

Typical instantaneous images for the forced jet at four different frequencies with azimuthal mode $m = \pm 1$ are shown in figure 7. It is clear from these and other images not shown here that the response is optimum for the generation of large-scale coherent structures and mixing enhancement at around 5 kHz (St_D of 0.33) and drops gradually above and below this value. These results are consistent with the earlier findings in low-speed and low-Reynolds-number flows (e.g. Crow & Champagne 1971; Hussain & Zaman 1981; Ho & Huerre 1984). As was discussed earlier, the preferred-mode Strouhal number varies significantly, from 0.2 to 0.6, showing relatively strong experimental facility dependence, but mostly seems to be around 0.3.

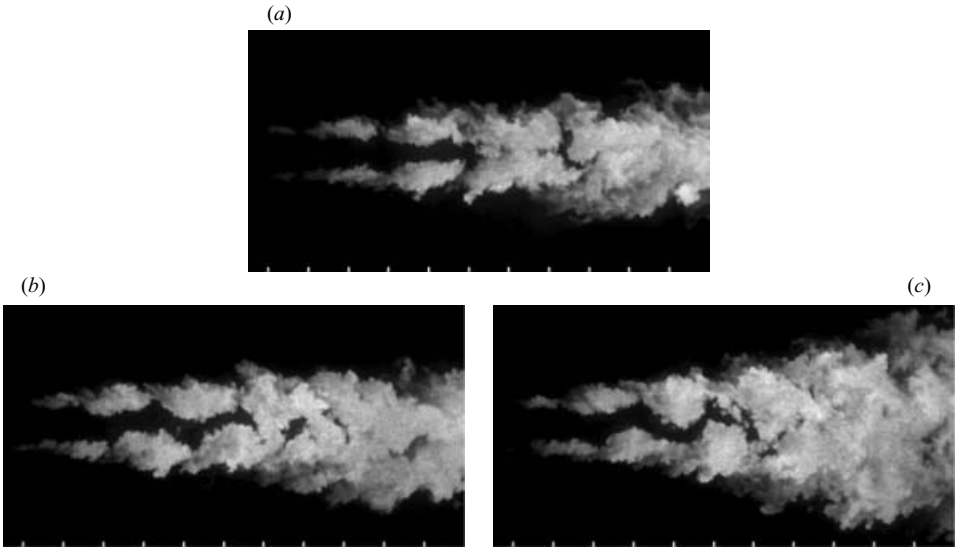

FIGURE 8. Instantaneous streamwise images for different azimuthal mode forcing at the preferred mode Strouhal number of 0.33. (*a*) Axisymmetric mode ($m=0$), (*b*) first helical mode ($m=1$), (*c*) flapping mode ($m=\pm1$).

Figure 8 shows instantaneous images of the jet forced at the preferred-mode Strouhal number of 0.33, but for three azimuthal modes: axisymmetric ($m=0$), first helical ($m=1$), and flapping ($m=\pm1$). One can see large-scale coherent structures, as in low-speed and low-Reynolds-number flows, which grow in the mixing layer in the downstream direction and interact with the structures in the other mixing layer towards the end of the *visual* potential core. Also, as it was expected, the structures are vertically/radially aligned in the axisymmetric forcing, but staggered in the first helical and the flapping modes forcing.

Figure 9 shows phase-averaged images of the jet corresponding to the instantaneous images shown in figure 8. The input signal to the actuator was used for phase locking and 30 phase-locked images were used to obtain each phase-averaged image. As can be seen, the structures are very well organized spatially. The fact that phase averaging produces such robust structures implies the structures must also be temporally coherent. The structures are oriented in response to the shear force in the jet and are quite round. This is consistent with the results of Hussain & Zaman (1981) who found the structures to become more round as the Reynolds number increases. The structures cannot be visualized close to the nozzle exit due to the lack of condensation and thus scattering particles. But the structure can be seen clearly from about $x/D\sim3$. There is no sign of pairing of the structures from this location to where structures begin to interact across or on the jet centreline. This agrees with the observations of Hussain & Zaman (1981) in low-speed and low-Reynolds-number jets. It can also be observed that the actuation perturbation growth ends and decay begins for forcing around the jet preferred mode for $m=0, 1, \pm1$ (figure 5*b*) approximately where the structures start interacting across or on the jet centreline (figure 9).

Figure 10 shows phase-averaged cross-stream images at $x/D=4$ of the jet forced with $m=\pm1$ at $St_{DF}=0.33$ over one complete forcing cycle (two consecutive images are $\pi/4$ apart; the order of the images is top row left-to-right, then bottom row left-to-right). The images show significant thickening and thinning in various parts

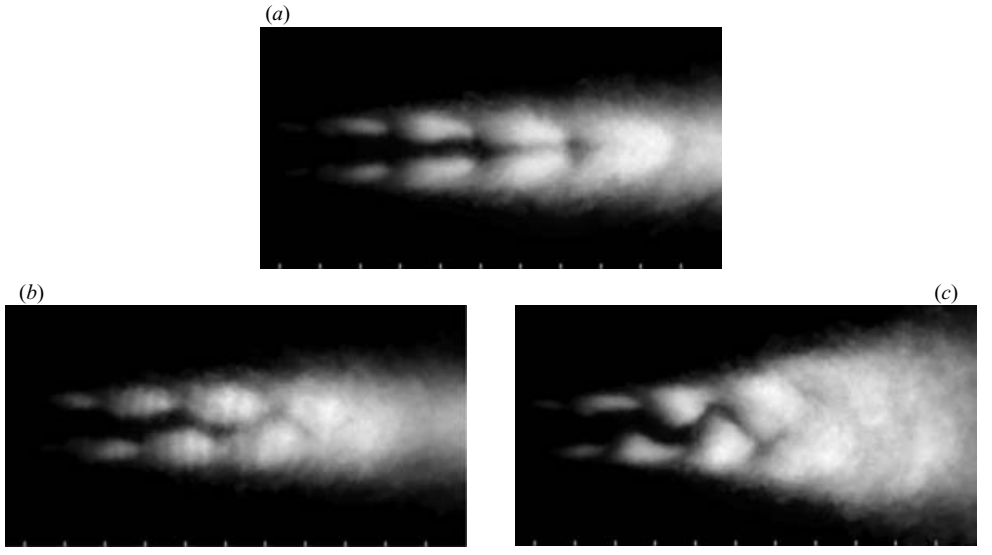

FIGURE 9. Phase-averaged images for the cases presented in figure 8: (*a*) $m = 0$, (*b*) $m = 1$, (*c*) $m = \pm 1$.

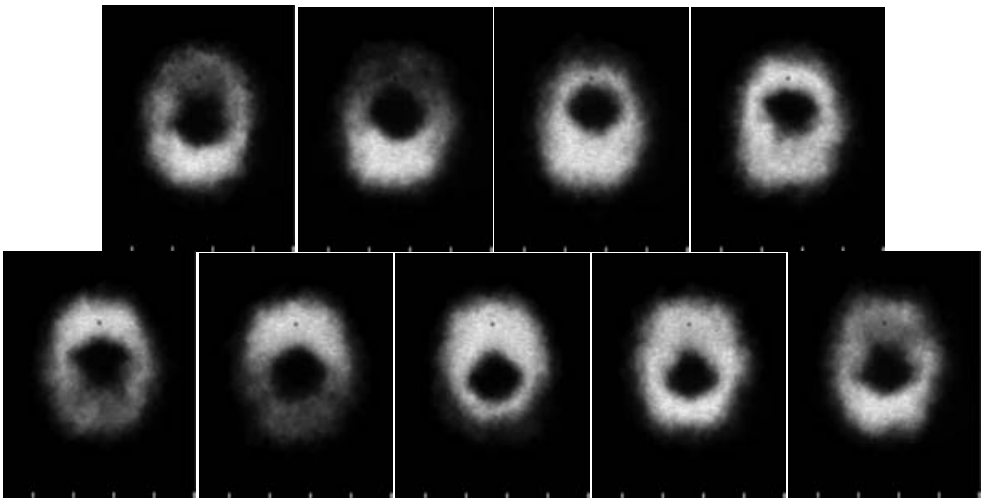

FIGURE 10. Cross-stream phase-averaged images for $m = \pm 1$ mode forcing at $St_{DF} = 0.33$ for one complete forcing cycle at $x/D = 4$. The order of images is top row (left-to-right), then bottom row (left-to-right).

of the mixing layer and also significant deformation of the jet core over a forcing period. These images, along with the streamwise images shown in figures 8(*c*) and 9(*c*), illustrate the complex and three-dimensional nature of the forced jet.

Two-dimensional spatial correlations obtained using the instantaneous images of the jet, such as those shown in figures 6–8, were used to investigate more quantitatively the periodic nature of structures in the baseline and the controlled jets and also to assess more objectively the effect of control on the jet. A small template, which covered the entire width of the top or bottom shear layer with a length slightly larger than the forcing wavelength in the streamwise direction, was selected, and the

two-dimensional spatial correlation between the image within the template and the rest of the image (of either top or bottom shear layer) was calculated. The two-dimensional spatial correlation is then averaged over 50 instantaneous images. Details of such a procedure can be found in Thurow *et al.* (2002). Briefly, the correlation technique utilizes the fluctuating scattered light intensity in the instantaneous images defined by

$$I'_k(x, y) = I_k(x, y) - \langle I(x, y)\rangle \tag{3.4}$$

where $I_k(x, y)$ is the scattered light intensity in the instantaneous image and $\langle I(x, y)\rangle$ is the ensemble-average of the scattered light intensity at that location over the 50 instantaneous images. Next, the two-dimensional spatial cross-correlation is performed to find the location of the structure in each subsequent frame. The normalized correlation, $r(i, j, k)$, for a $P \times Q$ template is then computed using

$$r(i, j, k) = \frac{\displaystyle\sum_{p=1}^{P}\sum_{q=1}^{Q}(I'(i+p, j+q, k))(J'(p, q))}{\left(\displaystyle\sum_{p=1}^{P}\sum_{q=1}^{Q}(I'(i+p, j+q, k))^2 \sum_{p=1}^{P}\sum_{q=1}^{Q}(J'(p, q))^2\right)^{1/2}}, \tag{3.5}$$

where J' is the fluctuating intensity within the template (I' is outside of template), i and j are indices in an $M \times N$ image, representing the streamwise and transverse shift of the template and respectively run from 0 to $M - P$ and $N - Q$, and k indicates the frame being searched. The normalized cross-correlation r is averaged over 50 images and it takes a value of $+1.0$ and -1.0 for perfect correlation and anti-correlation, respectively. If one picks a streamwise line (a fixed i) and converts the image pixel index j to a physical length, one can obtain a correlation profile along a line in the streamwise direction, corresponding to a fixed i.

Figure 11 shows the one-dimensional spatial correlation along a line in the streamwise direction passing through the peaks of the two-dimensional correlation for the baseline jet and several forced jets (different forcing frequencies, but all at the first helical mode $m = 1$). Note that the base level (the level about which the peaks and valleys fluctuate) for each curve depends on the selection of the template and the background intensity level. Thus, one should focus only on the differences between the amplitudes of peaks and valleys (i.e. correlation level) for each correlation curve. A sinusoidal profile with large amplitude indicates that the forcing generated robust periodic structures. Spatial correlation and thus spatial periodicity of the structures for the forced cases around the jet preferred mode frequency ($St_{DF} = 0.33$) are quite robust, as indicated by the strong correlation peaks and valleys. However, the spatial periodicity gradually decays away on either side of this frequency, and the correlations resemble that of the baseline case. The spatial wavelength of large-scale structures can be obtained from the spatial correlations (distance from peak-to-peak) in figure 11. This information can then be used along with the forcing frequency, as discussed below, to determine the convection velocity of the structures.

The convection velocity for the forced jet cases was calculated by multiplying the spatial wavelength of the structures (determined using the results in figure 11) by the forcing frequency. This technique can only be used for the forced cases for which the spatial wavelength can be calculated. The convection velocity normalized by the jet exit velocity, U_j, at several forcing Strouhal numbers between 0.20 and 0.66 and azimuthal modes, is shown in figure 12. The variation in the normalized convection velocity ranges from 0.6 to 0.72. Considering the accuracy of the calculations, it

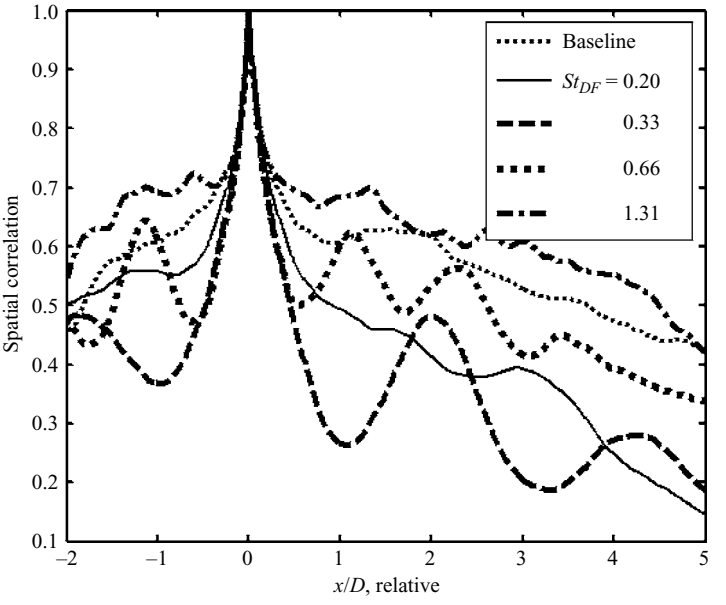

FIGURE 11. Image-intensity-based spatial correlation at various forcing frequencies for the helical mode ($m = 1$).

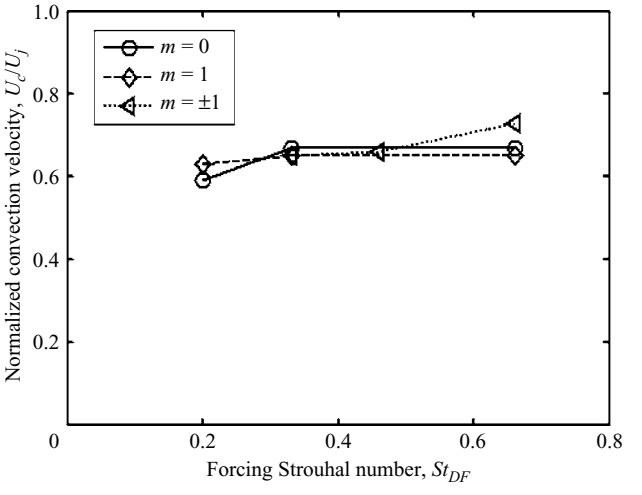

FIGURE 12. Normalized convection velocities for forcing various azimuthal modes.

seems that the normalized convection velocity does not depend on the forcing mode or frequency in a significant way. The present results agree quite well with those of Bridges (2006) measured in hot and cold unforced subsonic jets, which ranged from 0.6 to 0.7. Petitjean, McLaughlin & Morris (2006) measured a convection velocity of $0.77U_j$ in a Mach 1.76 unforced jet. For a Mach 2.1 jet forced using glow discharge, Troutt & McLaughlin (1982) measured a convection velocity of about $0.8U_j$ for a forcing Strouhal number of 0.3–0.8. It should be noted that the convection velocity varies across the jet shear layer and the results obtained by different methods would

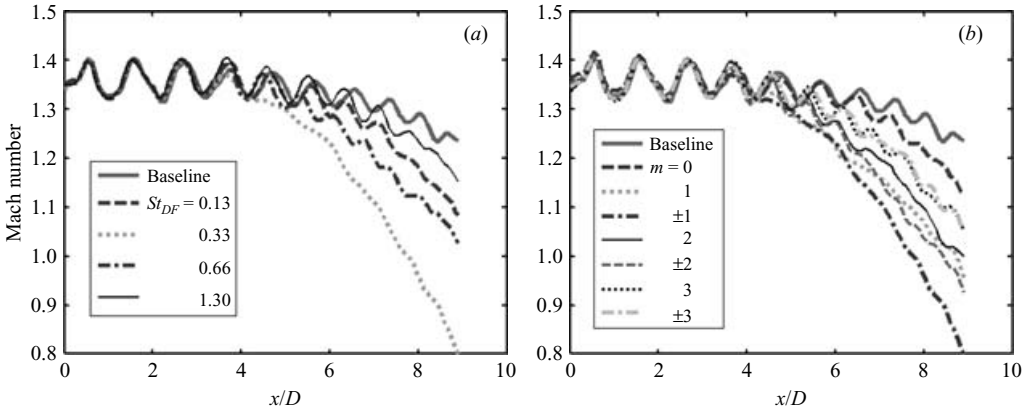

FIGURE 13. Jet centerline Mach number distributions for (*a*) several forcing frequencies with azimuthal mode $m = \pm 1$; and (*b*) several excitation modes at forcing $St_{DF} = 0.33$.

vary to some degree. Techniques using two-dimensional spatial correlations are more accurate than two-point spatial correlations.

3.4. *PIV results*

The flow visualization results presented above help in assessing the flow control effects and could also provide some quantitative data, such as spatial wavelength and convective velocity of large-scale structures, as discussed. They are qualitative in general, however, and must be evaluated and verified using more directly obtained quantitative measurements. For this purpose, we have used extensive PIV measurements, in addition to the actuation perturbation measurements.

Figure 13(*a*) shows the jet centreline velocity for the baseline case and for various forcing frequencies for the azimuthal mode $m = \pm 1$. As was shown earlier, forcing affects the jet over the entire forcing Strouhal number range of 0.13 to 1.3. But the effect is strongest around the jet preferred St_D of 0.33, as also shown in figure 7. Since the forcing is applied locally and only coupled into the shear layer, there is no forcing effect at the centreline until about 4 or 5 jet diameters downstream, where the shear layer has grown toward the jet centreline sufficiently and the structures have started to interact across the centreline. Lepicovsky, Ahuja & Burrin (1985) measured the centreline velocity of a low-speed and low-Reynolds-number jet excited at the preferred St_D and observed similar trends in the behavior of the jet core for the baseline and the forced cases. Over the first 4 jet diameters the centreline velocity for the forced cases were similar to the baseline, but around $x/D = 4$ the centreline velocity for the forcing cases began to decay while the baseline did not begin to decay until $x/D = 6$ to 8.

The current Mach 1.3 jet was operated as close to an ideally expanded jet as possible. Theoretically, there should not be any centreline Mach number variations in such a jet until the end of potential core, which is located approximately at $x/D = 6$ for the baseline jet and further upstream for the forced cases. We used the Method of Characteristics, which is an inviscid method, to design the nozzle. One can only approximately take into account the effect of the boundary layer growth within the nozzle. Therefore, there will always be weak compression and expansion waves in a supersonic jet. These waves become accentuated when the nozzle has a thick lip. In the current set-up, the nozzle extension, which holds the electrodes for the plasma actuators, acts like a very thick lip and accentuates these waves. The centreline

variations within the jet core in figure 13(*a*) and the subsequent figures are due to this phenomenon.

Forcing the jet at all Strouhal numbers causes a reduced jet potential core and an increase in the decay rate of the centreline Mach number of the jet beyond the end of potential core. These changes are much more dramatic for the preferred-mode Strouhal number case – an indication of substantial mixing enhancements that were also shown in the flow visualization results. When figures 4(*c*), 7, and 13(*a*) are compared, it becomes clear that the perturbation level significantly decreases downstream of the streamwise location where the generated large structures begin to interact. In figure 4(*c*), the perturbation level decreases noticeably at $x/D = 5$ and 8 for $St_{DF} = 0.33$ and 0.20, respectively. These streamwise locations roughly correspond to where the structures begin to interact (figure 7) and the centreline Mach number decay becomes visible (figure 13*a*). Results for $St_{DF} = 0.20$ are not shown, but they are close to those for $St_{DF} = 0.13$. Thus, all three different data sets confirm and complement each other.

Figure 13(*b*) shows the effects of forcing of the jet with various azimuthal modes at the jet preferred Strouhal number of 0.33. The results show that forcing the jet at all the modes from $m = 0$ to $m = \pm 4$ affects the jet to some degree, in agreement with the flow visualization results. The results are also in agreement with the instability analysis and experimental results in the literature that, for a thin incoming boundary layer ($D/\theta \sim 250$ in the present case), the jet responds to all lower azimuthal mode disturbances (e.g. Cohen & Wygnanski 1987; Corke & Kusek 1993). The axisymmetric mode forcing is the least and the $m = \pm 1$ mode the most effective, and all the others fall in between these two cases. One exceptional case is $m = 1$ (the first helical or spinning mode case), which has comparable effect to that of $m = \pm 1$ up to $x/D = 6$, beyond which the effect is significantly reduced. It is interesting to see that the centreline Mach number decay for $m = 0$ is very different from that for $m = 1$, although the development of the actuation perturbation for these two modes are almost the same as shown in figure 5(*b*). The phase-averaged images for these cases (figure 9) show that the generated large-scale structures cross the jet centreline for the $m = 1$ mode to interact with the structures on the other side, while the structures begin to interact on the centreline for the $m = 0$ case due to their symmetric nature. In general, the centreline velocity decay is due to entrainment of the ambient fluid into the jet centreline. A further decay would also occur if the large structures cross the jet centreline as for $m = 1$ (and also for the $m = \pm 1$ mode). However, the centreline velocity decay by entrainment could also be partially offset by self-induction for the $m = 0$ mode. A combination of these effects may explain the differences in the decay of the centreline Mach number for the two cases.

As was also mentioned earlier, one has to be cautious in comparing the effects solely based on the centreline decay, as not all the modes are axisymmetric in the average sense, and such a comparison could be misleading. For example, the $m = 1$ mode is axisymmetric in the average sense, but the $m = \pm 1$ mode is quite asymmetric. In fact, the effect of forcing with the $m = \pm 1$ is much less on the orthogonal plane than that for which the flow visualization results are shown in figures 7–9.

Figure 14(*a*) shows the normalized centreline turbulent kinetic energy ($TKE = (\sigma_u^2 + \sigma_v^2)/U_j^2$), where σ_u and σ_v are the two measured standard deviations of the velocity fluctuations in the streamwise and transverse directions, respectively, for the baseline jet and the forced jet with the $m = \pm 1$ mode at various forcing frequencies. The trends are similar to those of the centreline Mach number shown in figure 13(*a*), except that forcing at the jet preferred mode St_D of 0.33 is even more effective than

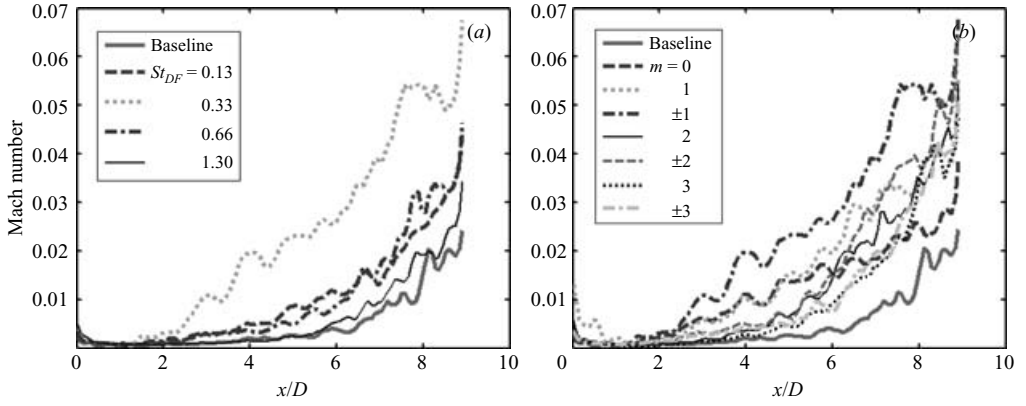

FIGURE 14. Turbulent kinetic energy along the jet centerline at (*a*) various forcing frequencies for forcing at azimuthal mode $m = \pm 1$; and (*b*) several forcing modes at forcing $St_{DF} = 0.33$.

all others in enhancing the mixing and increasing the centreline *TKE* level. Similar trends in centreline *TKE* when forcing the jet around the preferred St_D have also been seen in low-speed, low-Reynolds-number jets (Lepicovsky *et al.* 1985).

Figure 14(*b*) shows the normalized centreline turbulent kinetic energy for the baseline jet and the jet forced at $St_{DF} = 0.33$ with various azimuthal modes. The trends are to some degree similar to the ones shown for the centreline Mach number, except that the $m = 0$ mode forcing effect is similar to that of $m = 1$, but is reduced significantly farther downstream. Based on the results shown in figures 13(*b*) and 14(*b*) along with the explanation offered for the differences between the $m = 0$ and 1 cases, it appears that the centreline velocity fluctuations are governed primarily by the large structures crossing the jet centre. When more robust and energetic structures are generated and they penetrate deeper into the jet centreline, the centreline *TKE* develops faster as in the case of $m = \pm 1$ as shown in figure 8. Corke & Kusek (1993) also demonstrated in low-speed jets that when seeded with the $m = \pm 1$ mode, mixing was significantly enhanced in comparison to the other azimuthal modes. Since the structures generated near the preferred-mode Strouhal number are more robust, the centreline *TKE* increases as the forcing Strouhal number approaches 0.33 from either side as shown in figure 14(*a*). At a higher forcing Strouhal number, the generated structures are small and the interaction of these structures across the centreline is limited. As a result, the centreline velocity or Mach number decay becomes close to that for the baseline as the forcing frequency increases.

4. Concluding remarks

We have presented and discussed detailed experimental results on the control of high-speed and high-Reynolds-number jets. Excitation of such jets requires actuators that are capable of generating both high-amplitude and high-bandwidth control signals. Over the past couple of years, we have developed localized arc filament plasma actuators, which are suitable for such a task. We can drive many of these actuators with independent control of their frequency, phase, and duty cycle over a very wide band of frequencies (a few Hz to 200 kHz). The actuators are operated by an electronic input signal, which makes them ideal for both open- and closed-loop active flow control. Also, current and voltage measurements have demonstrated the

power consumption of each actuator to be quite low, a necessity in any control application.

In the present work, an axisymmetric Mach 1.3 jet with a Reynolds number based on the nozzle exit diameter of about 1.1×10^6 was forced using localized arc filament plasma actuators. Laser-based planar flow visualizations, actuation perturbation and instability wave/large-scale structures spatial development measurements, and two-component PIV measurements were used to evaluate the effects of forcing. Eight actuators distributed azimuthally inside the nozzle, approximately 1 mm upstream of the nozzle exit, were used to force various azimuthal modes over a large frequency range (St_{DF} of 0.13 to 1.3). The jet responded to the forcing over the entire range of frequencies, but the response was optimum (in terms of generating large-scale coherent structures and mixing enhancement) around the jet preferred-mode Strouhal number of 0.33 ($f = 5\,\text{kHz}$), in good agreement with the results in the literature for low-speed and low-Reynolds-number jets. The jet, with a thin boundary layer ($D/\theta \sim 250$), also responded to the various azimuthal modes explored ($m = 0$ to 3 and $m = \pm 1$, ± 2, ± 4), again in agreement with instability analysis and experimental results in the literature for low-speed and low-Reynolds-number jets. Forcing the jet with the azimuthal mode $m = \pm 1$ at the jet preferred-mode Strouhal number provided the maximum mixing enhancement, with a significant reduction in the jet potential core length and a significant increase in the jet centreline velocity decay rate beyond the end of potential core. The flow visualization, growth and decay of perturbation, and PIV data all together show that the plasma actuators have control authority over such a high-Reynolds-number and high-speed flow. These actuators with low power consumption, large amplitude and high bandwidth have opened up tremendous opportunities for control of high-speed and high-Reynolds-number flows in different applications including mixing enhancement and noise mitigation.

The support of this research by NASA Glenn Research Center and by the Ohio Department of Development is greatly appreciated. Discussions with James Bridges have always been fruitful.

REFERENCES

Adelgren, R. G., Elliott, G. S., Crawford, J. B., Carter, C. D., Donbar, J. M. & Grosjean, D. F. 2005*a* Axisymmetric jet shear-layer excitation induced by laser energy and electric arc discharges. *AIAA J.* **43**, 776–791.

Adelgren, R. G., Yan, H., Elliott, G. S., Knight, D. D., Beutner, T. J. & Zheltovodov, A. A. 2005*b* Control of Edney IV Interaction by pulsed laser energy deposition**.** *AIAA J.* **43**, 256–269.

Ahuja, K. K., Lepicovsky, J. & Burrin, R. H. 1982 Noise and flow structure of a tone-excited jet. *AIAA J.* **20**, 1700–1706.

Arakeri, V. H., Krothapalli, A., Siddavaram, V., Alkislar, M. B. & Lourenco, L. M.2003 On the use of microjets to suppress turbulence in a Mach 0.9 axisymmetric jet. *J. Fluid Mech.* **490**, 75–98.

Artana, G., D'Adamo, J., Leger, L., Moreau, E. & Touchard, G. 2002 Flow control with electrohydrodynamic actuators**.** *AIAA J.* **40**, 1773–1779.

Bobashev, S. V., Golovachov, Yu. P. & Van Wie, D. M. 2003 Deceleration of supersonic plasma flow by an applied magnetic field. *J. Propulsion Power* **19**, 538–546.

Bridges, J. 2006 Effect of heat on space-time correlations in jets. *AIAA Paper* 2006-2534.

Brown, G. L. & Roshko, A. 1974 On density effects and large structure in turbulent mixing layers. *J. Fluid Mech.* **64**, 715–816.

Callender, B., Gutmark, E. & Martens, S. 2005 Far-field acoustic investigation into chevron nozzle mechanisms and trends. *AIAA J.* **43**, 87–95.

Cohen, J. & Wygnanski, I. 1987 The evolution of instabilities in the axisymmetric jet. Part 1. The linear growth of disturbances near the nozzle. *J. Fluid Mech.* **176**, 191–219.

Corke, T. C. & Kusek, S. M. 1993 Resonance in axisymmetric jets with controlled helical-mode input. *J. Fluid Mech.* **249**, 307–336.

Corke, T. C. & Matlis, E. 2000 Phased plasma arrays for unsteady flow control. *AIAA Paper* 2000-2323.

Corke, T. C., Shakib, F. & Nagib, H. M. 1991 Mode selection and resonant phase locking in unstable axisymmetric jets. *J. Fluid Mech.* **223**, 253–311.

Crighton, D. G. & Gaster, M. 1976 Stability of slowly diverging jet flow. *J. Fluid Mech.* **77**, 387–413.

Crow, S. & Champagne, F. 1971 Orderly structure in jet turbulence. *J. Fluid Mech.* **48**, 547–591.

Gutmark, E. & Ho, C.-M. 1983 Preferred modes and the spreading rates of jets. *Phys. Fluids* **26**, 2932–2938.

Gutmark, E. J., Schadow, K. C. & Yu, K. H. 1995 Mixing enhancement in supersonic free shear layer flows. *Annu. Rev. Fluid Mech.* **27**, 375–417.

Henderson, B., Kinzie, K., Whitmire, J. & Abeysinghe, A. 2005 The impact of fluidic chevrons on jet noise. *AIAA Paper* 2005-2888.

Henoch, C. & Stace, J. 1995 Experimental investigation of a salt water turbulent boundary layer modified by an applied streamwise magnetohydrodynamic body force. *Phys. Fluids* **7**, 1371–1383.

Hileman, J. & Samimy, M. 2006 Mach number effects on jet noise sources and radiation to shallow angles. *AIAA J.* **44**, 1915–1918.

Hileman, J., Thurow, B. S., Caraballo, E. J. & Samimy, M. 2005 Large-scale structure evolution and sound emission in high-speed jets: real-time visualization with simultaneous acoustic measurements. *J. Fluid Mech.* **544**, 277–307.

Ho, C.-M. & Huang, L.-S. 1982 Subharmonics and vortex merging in mixing layers. *J. Fluid Mech.* **119**, 443–473.

Ho, C.-M. & Huerre, P. 1984 Perturbed free shear layers. *Annu. Rev. Fluid Mech.* **16**, 365–424.

Hussain, A. K .M. F. & Zaman, K. B. M. Q. 1980 Vortex pairing in a circular jet under controlled excitation. Part 2. Coherent structure dynamics. *J. Fluid Mech* **101**, 493–544.

Hussain, A. K. M. F. & Zaman, K. B. M. Q. 1981 The 'preferred mode' of the axisymmetric jet. *J. Fluid Mech.* **110**, 39–71.

Jubelin, B. 1980 New experimental studies on jet noise amplification. *AIAA Paper* 80-0961.

Kastner, J., Hileman, J. & Samimy, M. 2004 Exploring high-speed axisymmetric jet noise control using Hartmann tube fluidic actuators. *AIAA Paper* 2004-0186.

Kibens, V. 1980 Discrete noise spectrum generated by an acoustically excited jet. *AIAA J.* **18**, 434–451

Kibens, V., Dorris III, J. & Smith, D. M. 1999 Active flow control technology transition: the Boeing ACE Program. *AIAA Paper* 99-3507.

Krothapali, A., Venkatakrishnan, L, Lourenco, L, Greska, B. & Elavarasan, R. 2003 Turbulence and noise suppression of a high-speed jet by water injection. *J. Fluid Mech.* **491**, 131–159.

Leonov, S., Bityurin, V., Savelkin, K. & Yarantsev, D. 2002 Effect of electrical discharge on separation processes and shocks position in supersonic airflow. *AIAA Paper* 2002-0355.

Leonov, S., Bityurin, V., Yarantsev, D. & Youriev, A. 2003 The effect of plasma induced separation. *AIAA Paper* 2003-3853.

Leonov, S., Yarantsev, D., Kuryachii, A. & Yuriev, A. 2004 Study of friction and separation control by surface plasma. *AIAA Paper* 2004-512.

Lepicovsky, J., Ahuja, K. K & Burrin, R. H. 1985 Tone excited jets, Part III: Flow measurements. *J. Sound Vib.* **102**, 71–91.

Lepicovsky, J. & Brown, W. H. 1989 Effects of nozzle-exit boundary-layer conditions on excitability of heated free jets. *AIAA J.* **27**, 712–718.

Lu, H. Y. 1983 Effect of excitation on coaxial jet noise. *AIAA J.* **21**, 214–220.

Macheret, S. O., Shneider, M. N. & Miles, R. B. 2004 Magnetohydrodynamic and electrohydrodynamic control of hypersonic flows of weakly ionized plasmas. *AIAA J.* **42**, 1378–1387

Mengle, V. G. 2000 Optimization of lobe mixer geometry and nozzle length for minimum jet noise. *AIAA Paper* 2000-1963.

Michalke, A. 1965 On spatially growing disturbances in an inviscid shear layer. *J. Fluid Mech.* **23**, 521–544.

Michalke, A. 1977 Instability of compressible circular free jet with consideration of the influence of the jet boundary layer thickness. *NASA TM* 75190.

Minucci, M. A. S., Toro, P. G. P., Oliveira, A. C., Ramos, A. G., Chanes, J. B., Pereira, A. L., Nagamatsu, H. M. T., & Myrabo, L. N. 2005 Laser-supported directed-energy "air spike" in hypersonic flow. *J. Spacecraft Rockets* **42**, 51–57.

Mishin, G .I., Serov, Y. L. & Yavor, I. P. 1991 Flow around a sphere moving supersonically in a glow discharge plasma. *Tech. Phys. Lett.* **17**, 413–416.

Moore, C. J. 1977 The role of shear-layer instability waves in jet exhaust noise. *J. Fluid Mech.* **80**, 321–367.

Morrison, G. & McLaughlin, D. 1979 Noise generation by instabilities in low-Reynolds-number supersonic jets. *J. Sound Vib.* **65**, 177–191.

Nishihara, M., Jiang, N., Rich, J. W., Lempert, W. R., Adamovich, I. V. & Gogineni, S. 2005 Low-temperature supersonic boundary layer control using repetitively pulsed MHD forcing. *Phys. Fluids* **17**, 106102.

Parekh, D. E., Kibens, V., Glezer, A., Wiltse, J. M. & Smith, D. M. 1996 Innovative jet flow control: mixing enhancement experiments. *AIAA Paper* 96-0308.

Paschereit C. O., Wygnanski, I. & Fiedler, H. E. 1995 Experimental investigation of subharmonic resonance in an axisymmetric jet. *J. Fluid Mech.* **283**, 365–407.

Petitjean, B. P., McLaughlin, D. K. & Morris, P. J. 2006 An experimental investigation of density gradient fluctuations in high-speed jets using optical deflectometry. *AIAA Paper* 2006-2533.

Plaschko, P. 1979 Helical instabilities of slowly divergent jets. *J. Fluid Mech.* **92**, 209–215.

Post, M. L. & Corke, T. C. 2004 Separation control on high angle of attack airfoil using plasma actuators. *AIAA J.* **42**, 2177–2184.

Reshotko, E. 1994 Boundary-layer instability, transition, and control. *AIAA Paper* 94-0001.

Reynolds, W. C. & Bouchard, E. E. 1981 The effect of forcing on the mixing-layer region of a round jet. In *Unsteady Shear Flows* (ed. R. Michel, J. Cousteix & R. Houdeville), pp. 402–411. Springer.

Reynolds, W. C., Parekh, D. E., Juvet, P. J. D. & Lee, M. J. D. 2003 Bifurcating and blooming jets. *Annu. Rev. Fluid Mech.* **35**, 295–315.

Roth, J. R., Sherman, D. M. & Wilkinson, S. P. 2000 Electrohydrodynamic flow control with a glow-discharge surface plasma. *AIAA J.* **38**, 1166–1172.

Saiyed, N. H., Mikkelsen, K. L. & Bridges, J. E. 2003 Acoustics and thrust of quiet separate-flow high-bypass-ratio nozzles. *AIAA J.* **41**, 372–378.

Samimy, M., Adamovich, I., Webb, B., Kastner, J., Hileman, J., Keshav, S. & Palm, P. 2004 Development and characterization of plasma actuators for high speed jet control. *Exps. Fluids* **37**, 577–588.

Samimy, M., Zaman, K. B. M. Q. & Reeder, M. F. 1993 Effect of tabs on the flow and noise field of an axisymmetric jet. *AIAA J.* **31**, 609.

Stromberg, J., McLaughlin, D. & Troutt, T. 1980 Flow field and acoustic properties of a Mach number 0.9 jet at a low-Reynolds-number. *J. Sound Vib.* **72**, 159–176.

Thurow, B., Hileman, J., Lempert, W. & Samimy, M. 2002 A technique for real-time visualization of flow structure in high-speed flows. *Phys. Fluids* **14**, 3449–3452.

Troutt, T. R. & McLaughlin, D. K. 1982 Experiments on the flow and acoustic properties of a moderate-Reynolds number supersonic jet. *J. Fluid Mech.* **116**, 123–156.

Utkin, Y. G., Keshav, S., Kim, J.-H., Kastner, J., Adamovich, I. V. & Samimy, M. 2007 Development and use of localized arc filament plasma actuators for high-speed flow control. *J. Phys.* D (to appear).

Winant, C. D. & Browand, F. K. 1974 Vortex pairing: the mechanism of turbulent mixing-layer growth at moderate Reynolds number. *J. Fluid Mech.* **63**, 237–252.

Zaman, K. B. M. Q. 1999 Spreading characteristics of compressible jets from nozzles of various geometries. *J. Fluid Mech.* **383**, 197–228.

Zaman, K. B. M. Q. & Hussain, A. K. M. F. 1980 Vortex pairing in a circular jet under controlled excitation. Part 1. General jet response. *J. Fluid Mech.* **101**, 449–491.

Zaman, K. B. M. Q. & Hussain, A. K. M. F. 1981 Turbulence suppression in free shear flows by controlled excitation. *J. Fluid Mech.* **103**, 133–159.

Zaman, K. B., Reeder, M. F. & Samimy, M. 1994 Control of an axisymmetric jet using vortex generators. *Phys. Fluids* **6**, 778–793.

Zavialov, I., Khorunzhenko, V., Starikovskaia, S., Starikovskii, A. & Saddoughi, S. 2005 Plasma control of boundary layer using low-temperature non-equilibrium plasma of gas discharge. *AIAA Paper* 2005-1180.